Arc-Jet Testing on HfB_2 - $TaSi_2$ Models: Effect of the Geometry on the Aerothermal Behaviour

A. Di Maso[1], R. Savino[*,1], M. De Stefano Fumo[1], L. Silvestroni[2] and D. Sciti[2]

[1] *Dipartimento di Ingegneria Aerospaziale, University of Naples "Federico II", P.le V. Tecchio 80, 80125 Naples, Italy*

[2] *ISTEC, Institute of Science and Technology for Ceramics, CNR, Via Granarolo 64, 48018 Faenza, Italy*

Abstract: Arc-jet experiments in high enthalpy hypersonic (Mach 3) non equilibrium flow were carried out on a HfB_2 composite with addition of 15 vol% $TaSi_2$, at temperatures exceeding 2000 K. The aerothermal behaviour was tested considering models having two different geometries, i.e. hemispheric and cone-shaped. The surface temperature and emissivity of the material were evaluated during the tests. Numerical computations of the nozzle flow were carried out in order to identify the flow conditions around the model and to analyze the details of thermal heating. The chemical-physical modifications were analysed after exposures. The surface emissivity changed from 0.85 to 0.5 due to surface oxidation. The maximum temperatures reached on the tip were strongly dependent on the sample geometry, being around 2300 K for the hemisphere and 2800 K for the cone. Post test SEM analyses confirmed an excellent stability for this HfB_2-based material.

Keywords: High enthalpy flow, ceramics, structural composites, high temperature testing, SEM micrography, thermal protection systems.

1. INTRODUCTION

Ultra-high temperature ceramics (UHTCs) are currently considered as emerging materials for aerospace applications [1-4]. The increasing attention on this class of materials is driven by the demand of developing re-usable hot structures as thermal protection systems (TPS) of re-entry vehicles characterized by sharp leading edges and therefore by large aerothermal heating. The sharp geometry allows to lower aerodynamic drag and to improve the flight performances and crew safety, due to the larger cross range and manoeuvrability along with more comfortable re-entry trajectories [5,6]. However, the sharp vehicles will have to withstand temperatures that may exceed 2000 K during re-entry. As available materials can not survive such extreme temperatures, new ones are required for advanced thermal protection systems, such as the UHTCs [1,3,4,6,7]. The most useful ground technique for exploring the high temperature behaviour is arc-jet testing. This method provides the best ground based simulation of a re-entry environment, in different ways. On one hand, it allows to explore the oxidation behaviour under extreme conditions. On the other hand, the materials response to large heat fluxes is evaluated through the determination of important parameters, such as emissivity and catalycity. High values of emissivity and low values of surface catalycity are desired as they reduce temperature gradients and thermal stresses in the structure, thus enabling the vehicle to operate under relatively high enthalpy flow conditions. So far, the most appealing materials from the point of view of the aerothermal behaviour are certainly ZrB_2-SiC and HfB_2-SiC ceramics. Recently, HfB_2-$MoSi_2$ composites have been tested in an arc jet facility at temperatures exceeding 2300 K showing excellent stability [8].

In this paper, arc-jet testing at temperatures between 2300 K and 2800 K is carried out on a newly developed HfB_2-based composite containing 15 %vol $TaSi_2$. It has been found [9] that this composition has very interesting High Temperature (HT) properties, such as a 4pt flexural strength of 600 MPa at 1773K, which suggests a good high temperature stability. Furthermore, it has been reported that the addition of $TaSi_2$ as secondary phase offers significant improvement for the oxidation resistance of ZrB_2-based composites [10-13].

In order to investigate the aerothermal behaviour, two different geometries are considered, hemispherical and conical, both important for the high speed aerodynamics. The experiments were conducted with an arc jet plasma wind tunnel which generates a high enthalpy flow (up to 20 Mj/kg) at Mach 3 in low atmospheric pressure (300 Pa). The operative envelope of the plant permits to simulate the actual thermal re-entry conditions. Microstructural modifications induced by high thermal loading are investigated and discussed. In addition, fluid dynamic numerical simulations (CFD) are carried out in order to identify the flow conditions around the models, to analyze the details of thermal heating and to compare them with experimental values.

2. EXPERIMENTAL

2.1. Material Processing and Characterization

Two models hemisphere and cone of HfB_2 -15 vol% $TaSi_2$ were selected for the arc-jet tests. Drawings of the

---

*Address correspondence to this author at the Dipartimento di Ingegneria Aerospaziale, University of Naples "Federico II", P.le V. Tecchio 80, 80125 Naples, Italy; Tel: 00390817683360; Fax: 00390817682351;
E-mail: raffaele.savino@unina.it

1874-1460/10

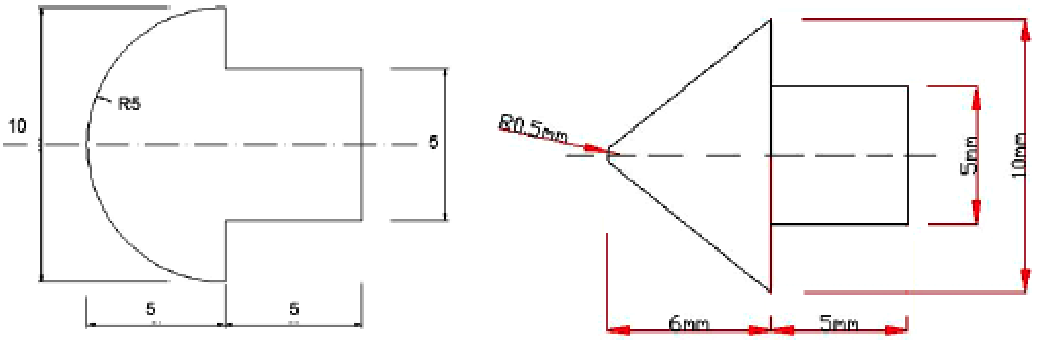

Fig. (1). Hemispherical and conical HfB_2-$TaSi_2$ models used for arc-jet testing.

models are shown in Fig. (**1**). Commercial powders were used to prepare the ceramic material: HfB_2 -325 mesh (Cerac Incorporated, Milwaukee, USA), $TaSi_2$ -45 µm (ABCR, GmbH & Co, Karlsruhe, Germany).

The powder mixtures were ultrasonically treated and then milled for 24 h in absolute ethanol using zirconia milling media. The mixed powders were dried in a rotary evaporator first and in a furnace at 340 K after, and then sieved in to -150 mesh screen size. A 3-cm diameter pellet was linearly pressed at 150 Kg/cm^2 and subsequently hot pressed at 2173K/15 min holding time in low vacuum with an applied pressure of 30 MPa. The sintered material was examined using X-ray diffraction (Siemens D500, Germany) to identify crystalline phases. Sections were polished with diamond paste to 0.25 µm and analyzed with scanning electron microscopy (SEM, Cambridge S360) and energy dispersive spectroscopy (EDS, INCA Energy 300, Oxford instruments, UK). After the arc jet tests, the ceramic models were further analysed by SEM-EDS on surface and polished cross-sections. A summary of the material features is reported in Table **1**.

Table 1. Starting Materials: Compositions, Densities and Mean Grain Size

Composition	Sintering Cycle	Bulk Density	Relative Density	M.g.s.
vol%	K/min	g/cm^3	%	µm
HfB_2+15 $TaSi_2$	2173/17	10.9	99.7	1

2.2. Arc-Jet Facility

Samples were exposed to high enthalpy flows using the Small Planetary Entry Simulator (SPES) arc-jet facility available at the Department of Aerospace Engineering of the University of Naples. SPES is equipped with a 80 kW plasma torch that operates in inert gas (He, N_2, Ar and their mixtures) at mass flow rates up to 5 g/s. In order to simulate air composition, O_2 can be added by means of a swirling jet in the mixing chamber after the torch. The nozzle has a throat diameter of 11 mm, an outer diameter of 22 mm and the nominal Mach number is M=3. The working pressure of the test chamber is between 100 and 500 Pa. During the experiments, infrared and optical windows in the test chamber allowed visual inspection and diagnostic analyses. An automatic control system monitored the main parameters of the apparatus (voltage and current of the arc heater, water cooling temperature, mass flow rate). In particular, the specific total enthalpy (H_0) was evaluated through an energy balance between the energy supplied to the gas by the arc heater and the energy transferred to the cooling system (measured by the water temperature jump between inlet and outlet). The output data, processed *via* a dedicated software, allowed the evaluation of the surface temperature profile versus exposure time of the model. Due to the extremely high thermal loading upon the ceramic models, surface chemical reactions, like oxidation, can be responsible for changes in the material's emissivity. To overcome this problem, the measurements were carried out with a radiation ratio pyrometer (Infratherm ISQ5, Impac Electronic Gmbh, Germany) which operates both in two colours and in the single colour function. In the two colours mode the instrument makes use of the ratio of two spectral radiances, measured at different wavelengths (0.9-1.05 µm), to evaluate the effective temperature. This overcomes the problem of the emissivity evaluation, since it is supposed to be the same at both wavelengths. Once the temperature had been measured with the ratio pyrometer, its value was input to evaluate the spectral emissivity using the single colour function (λ= 0.9 µm). In combination with the pyrometer, an infrared thermo-camera (Thermocam SC 3000, FLIR Systems, USA) was used to measure the surface temperature distributions and the spectral emissivity in the long wave range of the thermograph (λ=9 µm). It must be mentioned that in the present experiments the pyrometer was focused not on the models tip, but at an intermediate position, i.e. about 2.5 mm away from the hemisphere tip and 3 mm away from the cone tip. This implies that the actual tip temperature is much higher than that measured by pyrometer, as illustrated later in the paper.

2.3. Numerical Simulation of the Plasma Flow and of the Shock Layer Around the Model

Numerical computations were carried out in order to understand the aerothermal conditions of the experiments in the plasma wind tunnel. The wall heat fluxes, temperatures, pressures, and the chemical composition of the exit nozzle flow were calculated. The computations were carried out solving the full Navier-Stokes equations for a turbulent multi-reacting gas mixture with five chemical species (O, O_2, NO, N, N_2) in chemical non-equilibrium. Each species of the mixture was assumed to behave as a thermally perfect gas, where translational-rotational and vibrational-electronic degrees of freedom were characterised by different temperatures. The specific heat of gaseous species is constant because of the presence of vibrational-electronic energy [14-17].

The thermal conductivity and the viscosity is calculated by the kinetic theory. Vibrational-translational energy exchanges were modelled according to the Landau-Teller model, while the vibrational relaxation time was derived from the Millikan-White formula, with Park correction for high temperatures. Chemical and vibrational non-equilibrium was implemented using the Park model [14,18]. To speed up the numerical solution, the integration domain was divided in three parts. First, the fluid-dynamic problem was solved in the plasma torch, in the nozzle and test chamber. In the second step the fluid-dynamic field around the body was solved. In the third step, the results of the CFD computations, and in particular the heat flux distributions over the surface of the specimen, were used for the thermal analysis in order to evaluate the thermal field in the solid body of the specimen and the surface temperature distribution for the selected arc-jet conditions. In the present work, all the CFD simulations were carried out by imposing a zero catalytic efficiency for the boundary condition at the wall of the specimen [2-4,7,8,19]. The material properties used for numerical analysis are reported in Table **2**.

3. RESULTS AND DISCUSSION

3.1. Microstructural Features of the As-Sintered Sample

The XRD pattern (not shown) indicated that hexagonal HfB_2, hexagonal $TaSi_2$ and monoclinic HfO_2 were the crystalline phases present after sintering [9]. At high diffraction angles, splitting of the main reflections of HfB_2 was observed. These additional reflections were identified as a solid solution formed by the incorporation of Ta into the HfB_2 lattice with composition $(Hf_{0.8}Ta_{0.2})B_2$. A fine microstructure with little porosity (<1%) was observed in the polished surface (Fig. **2a**). The mean HfB_2 grain size was around 1 µm, which was similar to the starting particle size of the HfB_2 powder, indicating that no significant grain coarsening occurred during sintering. The brightest phase was identified as HfO_2 in agreement with the findings of the X-ray diffraction pattern. $TaSi_2$ appeared darker than HfB_2 (Fig. **2b**). Analyzing the microstructure in BSE imaging, many HfB_2 grains exhibited a core-shell structure (Fig. **2b**). By EDS analysis, the outer shell was estimated to be a solid solution with composition $(Hf_{0.8}Ta_{0.2})B_2$ in agreement with XRD analyses.

Table 2. Material Properties in the Numerical Model

Material	Density	C_p	Thermal Conductivity	Emissivity
%vol	g/cm^3	j/(kgK)	w/(mK)	
HfB_2+15 $TaSi_2$	10.9	400	78	0.8
HfO_2	10.9	400	2.5	0.6-0.5

3.2. Arc-Jet Tests

The arc-jet mass flow rate was set to simulate air. 1 gr/s with a chemical composition of 80 wt% N_2 and 20 wt% O_2. The specimens were located at a distance of 1 cm from the exit nozzle (Fig. **3**). The models were tested in a series of runs. Each run is constituted by a succession of steps

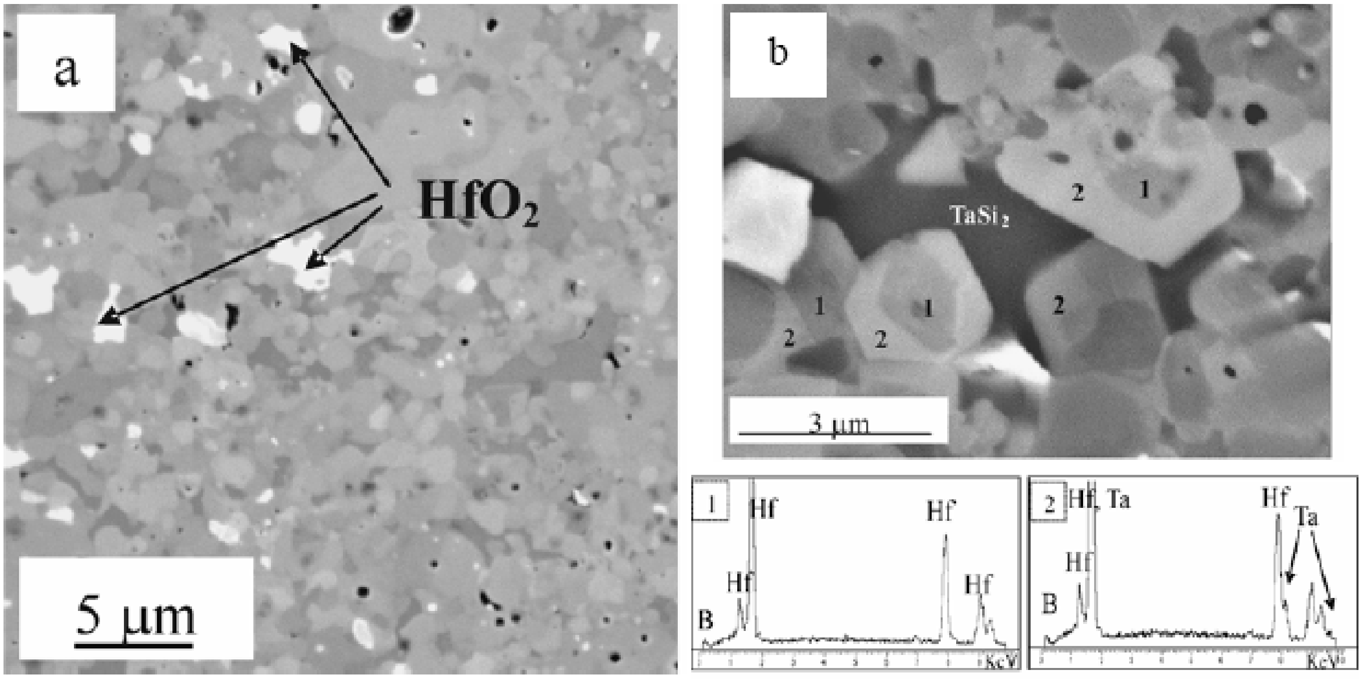

Fig. (2). Polished surfaces of as sintered HfB_2- $TaSi_2$ composite showing in **a**) the homogeneous and dense microstructure. **b**) Detail of the microstructure evidencing a pocket of $TaSi_2$ phase and the core-rim substructure of HfB_2 grains with the corresponding EDS spectra.

obtained by subsequent increase of the arc current. The initial average specific total enthalpy of about 8.7 MJ/kg was increased up to 12.9 MJ/kg. Table **3** shows the tests conditions and the stationary temperatures achieved. The stagnation point pressure in the present test conditions are between 7000 and 11000 Pa. Fig. (**4**) shows the thermal histories of the two models in the various runs and steps. The spectral emissivity measurements at 1 μm wavelength are plotted in Fig. (**5**). The emissivity plot shows that during the first run there is an abrupt decrease when the recorded temperature exceeds 1800K (from 0.85 at 1800 K to 0.45 at 2050K). In contrast, during the following runs, the values of emissivity tend to remain between 0.5 and 0.6. This change is certainly related to the microstructural modification induced by oxidation, as described later. During the first exposition, the high surface temperature achieved, together with the chemical environment, caused a surface oxidation, which changed the emissivity and the thermo-physical properties of the external layers. It must be mentioned that the temperature reached at the sample surface depends mainly on the ability of the material to reject the heat by radiation, i.e. on its emissivity ($\varepsilon = 1$ for an ideal black body, $\varepsilon < 1$ for a real material surface). The higher the emissivity, the greater the emitted radiation, the lower is the heating. The temperature distribution on the sample also depends on its thermal conductivity, since a high thermal conductivity allows heat to be conducted from the leading edge to colder zones and to obtain a more uniform temperature distribution.

At the exit of the torch, the plasma flow containing nitrogen and atomic nitrogen expands through the mixing chamber (22 mm in diameter), comes into contact with the oxygen, so that oxygen dissociates and a reacting mixture composed of O_2, N_2, NO, O and N is formed. Fig. (**6**) shows composition of the flow at the exit nozzle that results from computations performed considering a torch power of 16 and 29 KW, which corresponds to an average specific total enthalpy of 8.7 (condition (a) in Table **3**) and 12.9 MJ/kg respectively (condition (e) in Table **3**). According to the calculations, the average specific total enthalpy in proximity of the specimen remains constant with the same values as at the exit nozzle, at about 10 and 16 Mj/kg respectively. The mass fraction of dissociated oxygen is about 0.08 in the highest enthalpy condition, this dissociated oxygen is fundamental for the model oxidization, because of its reactivity. The far field pressure of the flow impacting the model has a value of around 1000 Pa. The stationary temperatures obtained by the numerical model are in a good agreement with the experimental ones, by assuming a non catalytic surface behaviour. The calculated wall heat flux distribution with cold wall (300 K) for the condition (e) is shown in Fig. (**7**). The average wall heat flux is larger for the conical geometry, but the integral of the wall heat flux is the

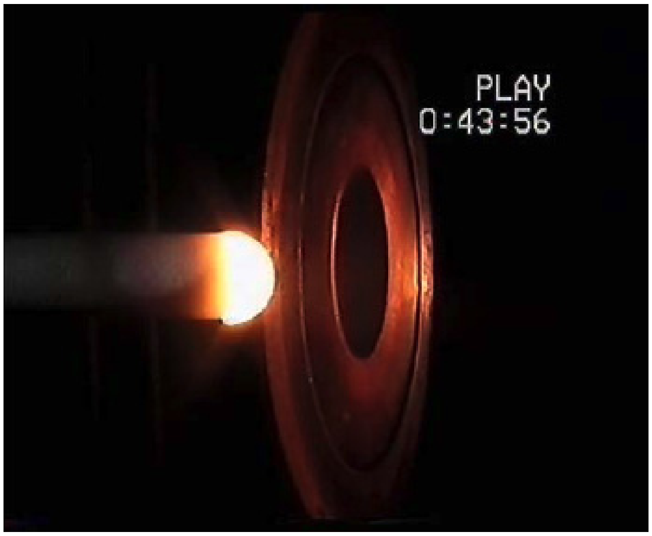

Fig. (3). An image of the experimental setup during the test.

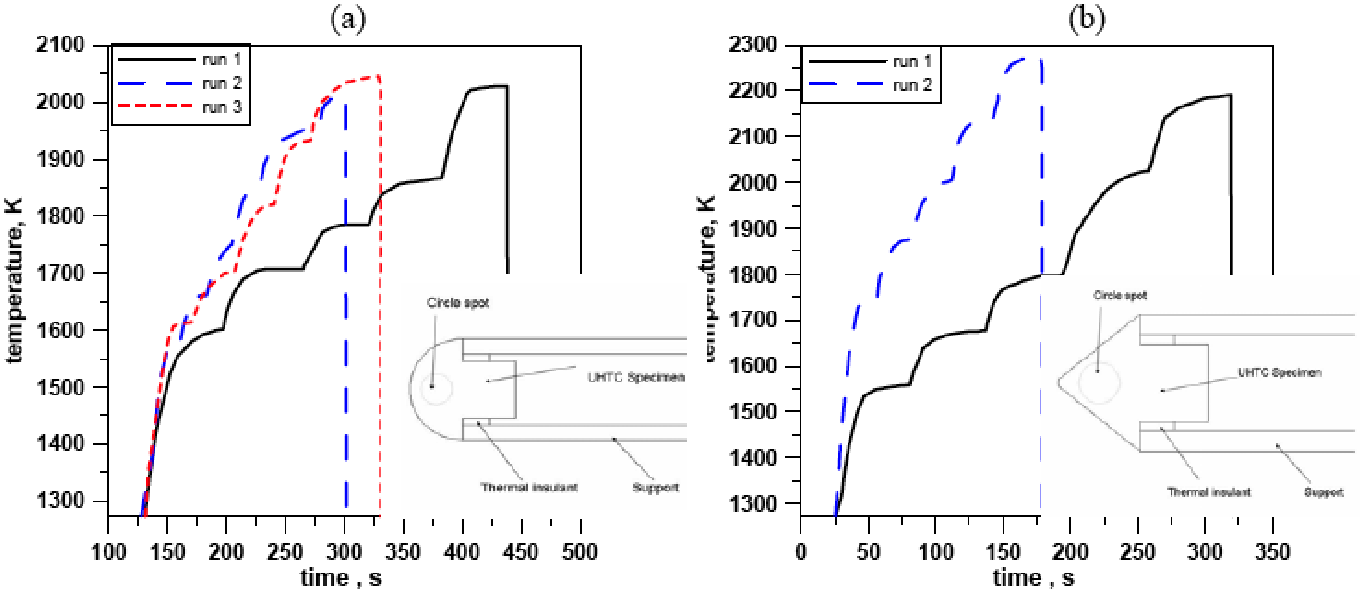

Fig. (4). Temperature histories *vs* time during arc-jet testing of the (**a**) hemisphere and (**b**) conic models. The pyrometer is focused on a 3mm diameter spot set around to the middle of the lateral surface.

same because of the larger surface area of the hemisphere. Fig. (**8**) shows the calculated increase of the surface temperature as a function of the exposition time for hemispheric and conic samples in the condition of step (e). The temperature on the leading edge increases rapidly and achieves the stationary state in few seconds. This is especially true for the cone, where the nose tip zone remains at high temperatures for a longer time than the base. The thermal heating is faster for the cone than for the hemisphere due to the lower mass of the former. The maximum temperature measured on the surface of the hemispherical sample was 2044 K (Fig. **4**), the total time of exposition was about 11 minutes. The corresponding stagnation point heat flux, computed by numerical simulation is in the range 3-6 MW/m^2.

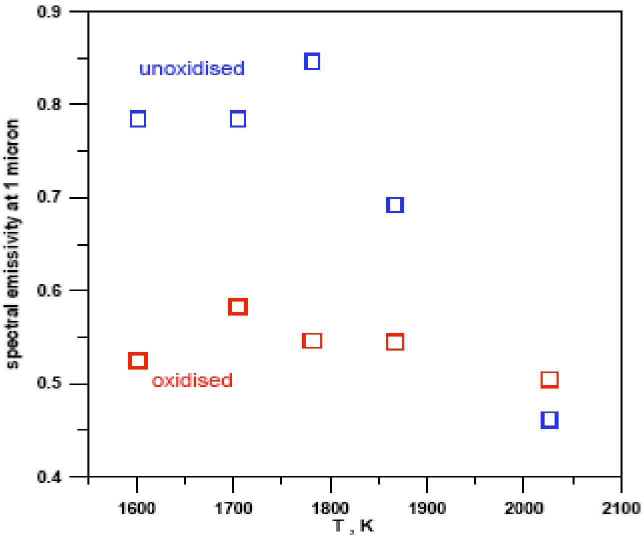

Fig. (5). Spectral emissivity at 1 µm *vs* temperature of the HfB_2-$TaSi_2$ model.

Table 3. Tests Conditions

	Condition	a	b	c	d	e
	Arch Power, kW	16000	19000	22000	26000	29000
	H0, Mj/kg (±10%)	8,71	8,96	9,77	11,69	12,90
Hemisphere	Tmax 1st run, K	1601	1705	1782	1867	2026
	Tmax 2nd run, K	1659	1747	1860	1958	2010
	Tmax 3rd run, K	1605	1701	1818	1931	2044
	Time exposition, s	142	129	111	116	186
Cone	Tmax 1st run, K	1558	1676	1794	2025	2182
	Tmax 2nd run, K	1733	1874	2011	2144	2279
	Time exposition, s	84	86	87	95	95

During the test, the cone surface temperature measured by the two colour pyrometer reached 2279 K, the total time of exposition was about 8 minutes. The corresponding computed stagnation point wall heat flux is of the order of 6-13 MW/m^2.

The formation of the oxide layer with a low thermal conductivity can create a change in the temperature distribution. To assess if such oxidised layer can generate a significant change in the surface temperature, a numerical model of the cone and of the hemisphere with a mixed oxide layer HfO_2 and SiO_2 was implemented. From the post exposure analysis (see next paragraph), the oxide thickness is variable from 170 to 100 µm for the cone and from 130 to 45 µm for the hemisphere. In first approximation, the oxide was considered to be constituted by a mixture of 50 vol%

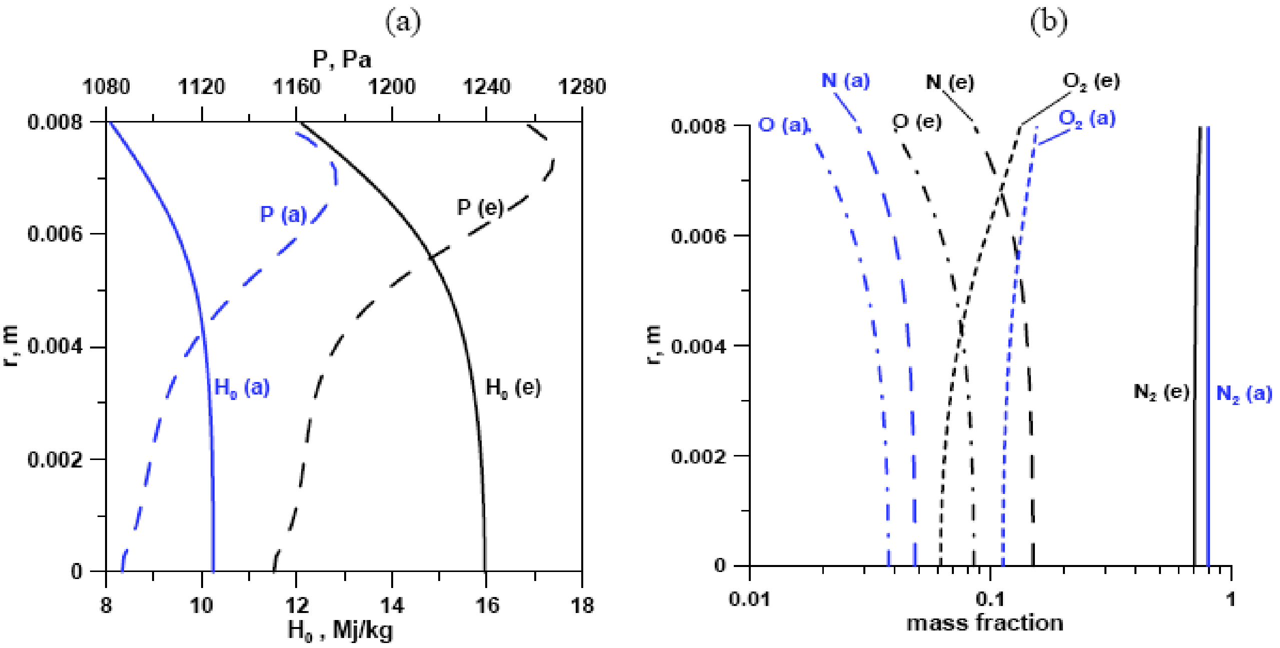

Fig. (6). a) Computed pressure and total enthalpy and **b**) computed mass fractions of the species along the exit nozzle for conditions (a) and (e) indicated in Table **3**.

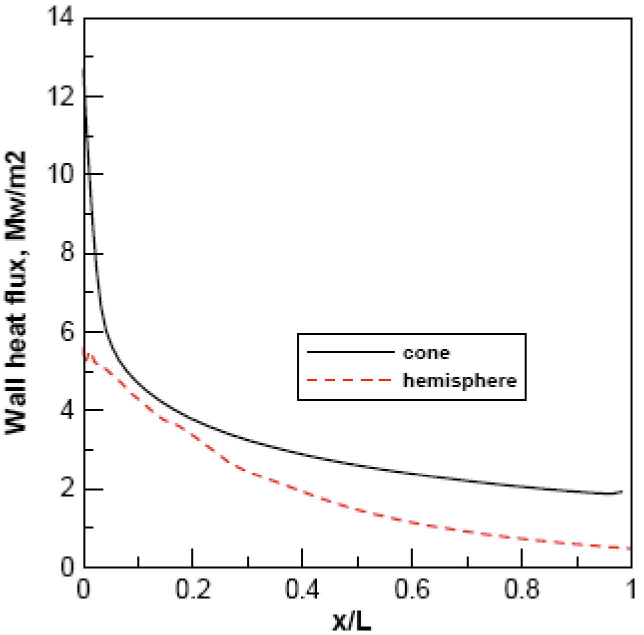

Fig. (7). Calculated wall heat flux on the models' surfaces, for the worst thermal condition, i.e. for the step (e) in Table **3**.

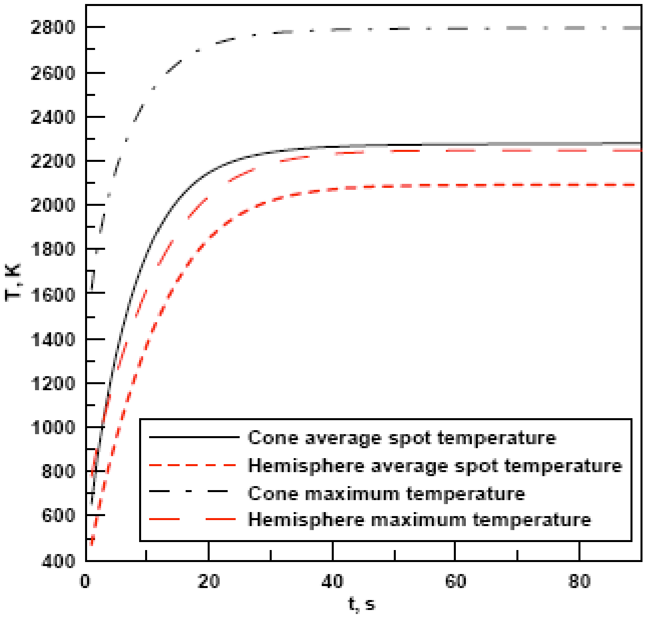

Fig. (8). Numerical temperature histories of the models surfaces in the case of the wall heat flux corresponding to point (e) of Table **3**. For oxidised surfaces, the emissivity was considered 0.5.

HfO_2+50 vol% SiO_2, taking 1.6 W/(mK) and 3.3 W/(mK) as the thermal conductivities of silica [20] and HfO_2 [21] respectively. Hence an average thermal conductivity value of 2.5 W/(mK) was used.

The resulting surface temperature profiles are shown in Fig. (**9**) and compared to the surface temperatures of a non oxidised material. The points corresponding to the experimental temperatures are also superimposed to the curves, showing a good agreement with the simulations. The surface temperature distribution of the oxidised layer is radically different from that of unoxidised model, especially in the tip region (Fig. **9**). Indeed for the cone, the increase of the maximum temperature reached on the tip due to oxidization is about 400 K respect to that of unoxidised model. Instead, for the hemisphere, the difference between the oxidised and unoxidised model is about 85 K. This can be explained with a thinner oxide layer for the hemisphere than for the cone. The change of temperature distribution caused by the oxide formation does not have a significant effect on the experimental temperature read by pyrometer. As a matter of fact, the increase of temperature due to oxidization is located only in the leading edge, while the pyrometer reads the average temperature in a spot at around in the middle height of the specimen body. On the contrary, the high temperature resulting by the numerical simulation on the leading edge of the oxidised cone must be taken into account, because it could be responsible for more pronounced damages on the top of the cone surface.

3.3. Microstructural Modifications Induced by High Enthalpy Plasma

The hemisphere model was subjected to three thermal cycles from room temperature to the final temperature in about 300-400 s. For each run, the maximum temperature was held for about 180 s. According to the computed simulations, the tip of the model reached a temperature of about 2200 K. The altered morphology of the hemisphere after arc jet testing is shown in Fig. (**10**). The sample surface was covered by an amorphous silica-based scale, which embedded elongated crystals (Fig. **10a**, **b**). XRD pattern (not shown) revealed that the crystalline phases present after thermal treatment are prevalently a mixed oxide with stoichiometry $Ta_2O_5{\cdot}6HfO_2$ and traces of HfO_2. The composition of the outer glassy layer was also investigated by means of EDS analysis. The silica-based scale contained several impurities, including Ta and Hf (see EDS spectrum in Fig. **10c**). The presence of boron is more difficult to track, due to the low sensitivity of energy-dispersive spectroscopy to light elements. Pores formation observed on the surface was due to evolution of gaseous products. The analysis of the cross section (Fig. **10c**) revealed that the scale was a multilayered oxide having a variable thickness (130 µm in the near-tip region, 50 µm in the back). Despite the presence of few macro-cracks at the interface between oxide and unreacted bulk, the scale was quite well adherent to the bulk. According to EDS analysis, the outer layer is constituted by a mixed Hf, Ta -oxide dispersed in the above mentioned Ta-containing silica amorphous layer (Fig. **10c**). The EDS quantitative elemental analysis indicates that elongated grains are the $Ta_2O_5{\cdot}6HfO_2$ phase detected by XRD diffraction. Underneath this layer, the scale was mainly constituted by porous HfO_2 in form of large rounded grains (~5 µm) containing a low amount of Ta (less than 3 at%). Finally, the inner layer was composed of fine HfO_2 grains (<2 µm) and residual porosity. Few silica was observed in the intermediate and inner layers. Due to the severe conditions applied and the thermal cycling, micro-cracks were observed in both Hf, Ta-oxide and HfO_2 phases.

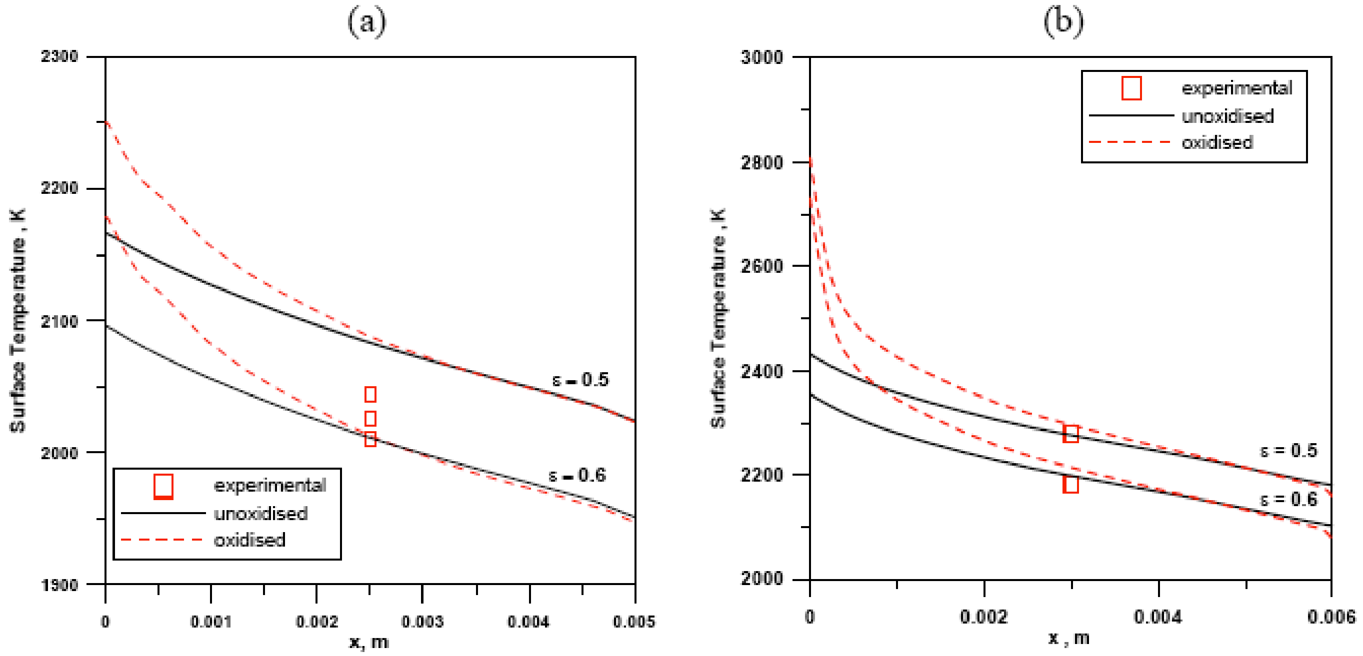

Fig. (9). Computed surface temperature distribution for the condition at point (e), for the hemisphere (**a**) and cone (**b**). Emissivity of 0.5 and 0.6 were considered for oxidised and non oxidised surface, respectively. Experimental value are superimposed.

The cone model was subjected to 2 cycles from room temperature to the final temperature in about 150 s. For each run, the maximum temperature was held for about 90 s. According to numerical simulations, the maximum temperature on the tip was of order of 2800 K and rapidly decreased along the cone profile (Fig. **9b**). The analysis of the sample surface revealed that the extent of damage was much more pronounced for this model, due to the higher temperature reached, especially in the near-tip regions (compare Fig. **10a** to Fig. **11a**). During cutting and polishing operations, detachment of a portion of the tip scale occurred, indicating that this part of the scale was poorly bonded to the material bulk. The surface morphology was heavily altered by the shear forces associated to the hot stream, which enhanced the bursting of bubbles (Fig. **11a-c**). As for the previous case, the scale was a multilayered oxide having a variable thickness (~170 µm near the tip, ~100 µm in the bottom part). The outer layer is constituted by a mixed Hf, Ta-oxide with stoichiometry $(Hf_{0.8}Ta_{0.2})O_2$ dispersed in the above mentioned Ta-containing silica amorphous layer. Occasionally, a slight shoulder was observed on EDS patterns which could be attributed to presence of B. In this case, the thickness of the outer compact layer is much reduced compared to the overall scale thickness, less than 1/5 (Fig. **11d**). Underneath this oxide layer (Fig. **11e**), the scale was mainly constituted by large rounded HfO_2 grains (5 µm) containing a low amount of Ta (less than 3 at %) and large porosities. The presence of silica in this layer was dependent on the position. No silica was observed in the near-tip regions. Some silica was instead observed in the bottom regions (Fig. **11f**). Macro-cracks were observed at the interface oxide/unreacted bulk. The hafnium oxide crystals also presented micro-cracks (Fig. **11f**).

The observed morphologies evidence that the samples underwent complex oxidation phenomena. Hafnium diboride is known to oxidize according to:

$$HfB_2(s) + 5/2\ O_2\ (g) = HfO_2\ (s) + B_2O_3(l) \qquad (1)$$

$$B_2O_3(l) = B_2O_3(g) \qquad (2)$$

Hafnia is a very stable phase in oxidizing atmosphere above 2300 K. It has a melting point of 3173 K and relatively low vapour pressure [22]. HfO_2 in the pure form crystallizes in the monoclinic phase at room temperature, but transforms into the tetragonal phase over a temperature range of 373-2023 K, becoming fully tetragonal above 2023 K. This transformation is reversible and, during cooling, the return to the tetragonal phase is associated to a large volume change (3-4%) which can cause structural degradation, especially under repetitive thermal cycling. Thus, if the oxide is not stabilized with higher valence cations, cracking due to volume expansion is predictable. On the other hand, boron oxide has a low melting point and high vapour pressure, therefore at T>1373K, it starts to evaporate. Hence, the overall oxidation process of hafnium diboride is the result of the combined processes of oxygen inward or metal ion outward diffusion and, at relatively lower temperatures, gaseous/liquid products outward diffusion through the oxide scale.

Besides, $TaSi_2$ may oxidise according to:

$$2\ TaSi_2 + 6.5\ O_2(g) = Ta_2O_5 + 4\ SiO_2 \qquad (3)$$

At T >1973 K, the Ta-Si-O phase diagram [23] indicates formation of liquid phase. Another paper [22] reports that Ta_2O_5 is liquid at temperature >2073K. Thus the formation of liquid phase at the temperatures involved in the present experiments is confirmed.

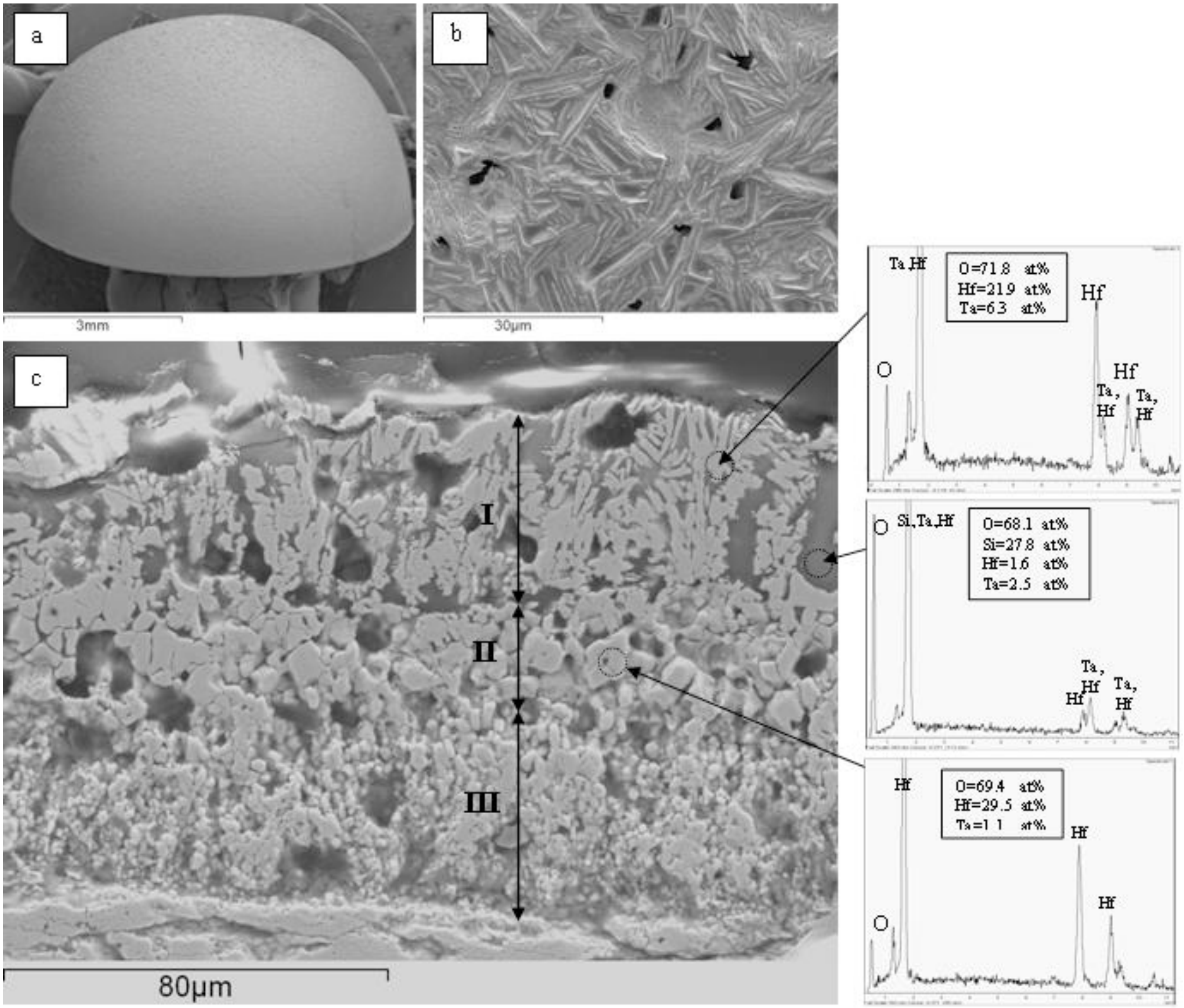

Fig. (10). **a**) Surface morphology of the hemisphere, **b**) detail showing $Ta_2O_5{\cdot}6HfO_2$ crystals in Ta-borosilicate glass on the model surface. **c**) Polished cross section showing the three layered scale and the corresponding EDS spectra on the right: I - $Ta_2O_5{\cdot}6HfO_2$ crystals/ Ta-borosilicate glass, II - large HfO_2 crystals after grain growth, III - fine grained HfO_2.

The morphology of the observed oxides suggests the following oxidation phenomena. As the temperature rises and overcomes 2073 K, a liquid Ta-Si-O phase is formed on the sample surface, whilst HfB_2 oxidises to HfO_2 and liquid/gaseous B_2O_3. The Ta-Si-O phase further reacts with newly formed HfO_2 crystals, leading to formation of the $Ta_2O_5{\cdot}6HfO_2$ crystals with elongated and dendritic morphology and a Ta- containing borosilicate glass. The $Ta_2O_5{\cdot}6HfO_2$ phase, which is not thoroughly investigated, can only be formed on the sample surface where the temperature is 1873 K or higher and where the Ta-Si-O phase is present. Indeed, this phase is not found in the intermediate and inner layers, which are depleted from the amorphous silica-based phase. As a confirmation, in the bottom regions of the sample, where the maximum temperature decreases, the $Ta_2O_5{\cdot}6HfO_2$ phase is not observed. The melting point of the $Ta_2O_5{\cdot}6HfO_2$ phase is not known, i.e. it could be higher of lower than pure hafnium oxide.

The comparison between the oxide morphologies of the two models can give some more indications. In the cone, the external layer constituted by amorphous silica phase plus $Ta_2O_5{\cdot}6HfO_2$ phase in the near-tip region is less than 1/5 of the entire scale thickness. For the hemisphere, experiencing lower specific fluxes and temperatures (max temperature around 2300 K) the external layer is about 1/3 of the whole scale thickness. This indicates that at temperatures between 2300 and 2800 K, extensive evaporation of $Ta_2O_5{\cdot}6HfO_2$ occurs. This suggests that this new phase has a melting point which could be lower than that of pure HfO_2, 3173 K.

Overall, the effect of $TaSi_2$ addition can have positive and negative effects on the oxidation resistance of HfB_2. On one hand, $TaSi_2$ modifies the Si-based oxidation layer, forming a Ta-containing boro-silicate glass. Then, it induces

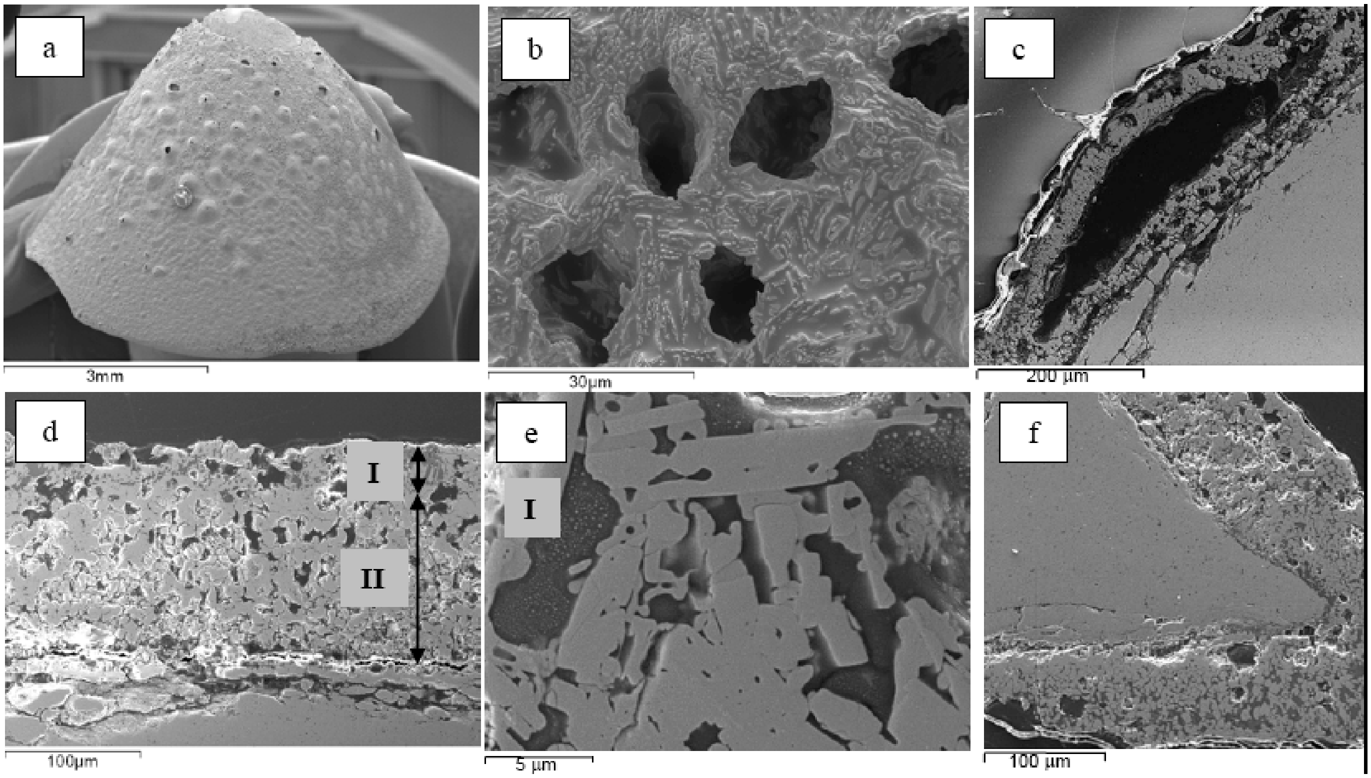

Fig. (11). **a**) Post test surface morphology of the cone, **b**) detail of the external surface, **c**) cross section showing scale spalling, **d**) cross section of the two layered scale, **e**) detail of the layer (I) constituted by $Ta_2O_5 \cdot 6HfO_2$ crystals in Ta-borosilicate glass, **f**) details of morphology in the bottom cone evidencing enlarged HfO_2 crystals dispersed in silica.

phase separation in the glass as evidenced by the crystallization of a $Ta_2O_5 \cdot 6HfO_2$ phase. Glass immiscibility has been reported to be one of the major cause for oxidation resistance improvement [24] for $TaSi_2$ containing UHTCs, due to increased viscosity which limits oxygen diffusion. It has been reported that the addition of $TaSi_2$ to ZrB_2-SiC composites largely improved their oxidation resistance at T<1900 and this could be due to Ta incorporation in the ZrO_2 lattice which can possibly give phase stabilization [12]. In the present case, the presence of micro-cracks in the HfO_2 crystals indicates that the Ta^{5+} cation could be not so effective in preventing the HfO_2 polymorphic transformation. The formation of the mixed $Ta_2O_5 \cdot 6HfO_2$ seems to be advantageous for temperatures up to 2300 K, as compact and dense textures of glassy and crystalline areas form. However, increasing the temperature to 2800 K, the outer protective layer starts to evaporate significantly as its melting point is likely to be lower than that of pure HfO_2.

CONCLUSIONS

Two different shapes of ultra-high temperature ceramics, HfB_2+15 vol% $TaSi_2$ were produced by hot pressing. The models were exposed to ground simulated atmospheric re-entry conditions using arc-jet testing, with an average specific total enthalpy of the flow around the body of the order of 9-13 MJ/kg. During the expositions, extensive oxidation of the constituent phases occurred, with formation of a compact surface layer constituted by $Ta_2O_5 \cdot 6HfO_2$ elongated crystals dispersed in a Ta-containing borosilicate glass. This in turns modified the surface emissivity of the samples from 0.85 to 0.55.

The starting geometry heavily affected the aero-thermal response of the models. According to calculations, for the hemisphere the maximum achieved temperature was of the order of 2300 K, for the nose cone the tip temperature reached 2800 K. Post test SEM analyses confirmed that the addition of $TaSi_2$ guarantees a good oxidation resistance for temperatures up to 2300 K, due to glass immiscibility and formation of a Ta-containing borosilicate glass. At T>2300 K, extensive evaporation of $Ta_2O_5 \cdot 6HfO_2$ phase/Ta-Si-O phase and oxide spalling occur.

Numerical calculations, which simulated the chemical non-equilibrium flow around the hemispherical model, are in good agreement with the experimental results assuming a non catalytic surface behaviour.

REFERENCES

[1] K. Upadhya, J.M. Yang, and W. Hoffman, "Materials for ultrahigh temperature structural applications", *Am. Ceram. Soc. Bull.*, vol. 76 (12), pp. 51-56, 1997.

[2] J. Marschall, A. Chamberlain, D. Crunkleton, and B. Rogers, "Catalytic atom recombination on ZrB_2/SiC and HfB_2/SiC ultrahigh-temperature 511ceramic composites", *J. Spacecraft Rockets*, vol. 41 (4), pp. 576-581, 2004.

[3] M. Gasch, D. Ellerby, E. Irby, S. Beckman, M. Gusman, and S. Johnson, "Processing, properties and arc-jet oxidation of hafnium diboride/silicon carbide ultra high temperature ceramics", *J. Mater. Scie.*, vol. 39, pp. 5925- 5937, 2004.

[4] A. Bongiorno, C. J. Forst, R. K. Kalia, J. Li, J. Marschall, A. Nakano, M.M. Opeka, I.G. Talmy, P. Vashishta, and S. Yip, "A perspective on modelling materials in extreme environments:

oxidation of ultrahigh-temperature ceramics". *MRS Bull.,* vol. 31, pp. 410-418, 2006.

[5] R. Janowski, M. Tauche, M. Scheper, R. Monti, and R. Savino, "Spaceplane: a new way for atmospheric reentry". *In Proceedings of the 1st Inter- national ARA Days, Atmospheric Reentry Systems, Missions and Vehicles*. Session 15-System Design, 2006.

[6] R. Monti, M. De Stefano Fumo, and R. Savino, "Thermal shielding of a reentry vehicle by ultra high temperature ceramic materials". *J. Thermophys. Heat Transf.*, vol. 20 (3), pp. 500-506, 2006.

[7] N. Richet, P. Lespade, P. Goursat, and E. Laborde, "Oxidation resistance of HfB2-SiC coatings for protection of carbon fiber based composites". *Key Eng. Mater*., 264-268 (TTP), pp. 1047-1050, 2004.

[8] R. Savino, M. De Stefano Fumo, L. Silvestroni, D. Sciti, "Arc-jet testing on HfB$_2$ and HfC-based ultra high temperature ceramic materials", *J. Eur. Ceram. Soc.,* vol. 28, pp. 1899-1907, 2008.

[9] D.Sciti, L. Silvestroni, G. Celotti, C. Melandri, and S. Guicciardi, "Sintering and mechanical properties of ZrB$_2$-TaSi$_2$ and HfB$_2$-TaSi$_2$ ceramic composites", *J. Am. Ceram. Soc.,* vol. 91, pp. 3285-3291, 2008.

[10] E. J. Opila, S. Levine, and J. Lorincz, "Oxidation of ZrB$_2$- and Hf B$_2$-based ultra-high temperature ceramics: effect of Ta additions", *J. Mater. Sci.,* vol. 39, no. 19, pp. 5969-77, 2004.

[11] I. G. Talmy, J. A. Zaykoski, M. M. Opeka, and A. H. Smith, "Properties of Ceramics in the System ZrB$_2$-Ta$_5$Si$_3$," *J. Mater. Res*., vol. 21, no. 10, pp. 2593-2599, 2006.

[12] S. R. Levine, and E. J. Opila, "Tantalum Addition to zirconium diboride for improved oxidation resistance," NASA/TM-2003-212483, 2003.

[13] Fei Peng, and Robert F. Speyer, "Oxidation resistance of fully dense ZrB$_2$ with SiC, TaB$_2$, and TaSi$_2$ additives", *J. Am. Ceram. Soc,* vol. 91, no. 5, pp. 1498-1494, 2008.

[14] C. Park, *Nonequilibrium Hypersonic Aerothermodynamics*, New York: John Wiley &Sons, 1990.

[15] C. Park, "Review of chemical-kinetic problems of future NASA missions", *J. Thermophys. Heat Transf.*, vol. 7, no. 3, pp. 385- 398, 1993.

[16] C. Park, J. T. Howe, R. L. Jaffe, and G. V. Chandler, "Review of chemical-kinetic problems of future NASA missions. II. Mars entries", *J. Thermophys. Heat Transf.*, vol. 8, no. 1, pp. 9-23, 1994.

[17] C. Park, R. L. Jaffe, and H. Partridge, "Chemical-kinetic parameters of hyperbolic earth entry", *J. Thermophys. Heat Transf.*, vol. 15, no. 1, pp. 76- 90, 2001.

[18] R. C. Millikan, D. R. White, "Systematics of vibrational relaxation", *J. Chem. Phys.*, vol. 39, no. 12, pp. 3209-3213, 1963.

[19] L. Scatteia, R. Borrelli, G. Casentino, E. Beche, J.L. Sans, and M. Balat-Pichelin, "Catalytic and radiative behaviours of ZrB2-SiC ultrahigh temperature ceramic composites", *J. Spacecr. Rockets*, vol. 43, pp. 1004-12, 2006.

[20] R. Morrell, *"Handbook of Properties of Technical and Engineering Ceramics"*, Part 2: Data Reviews, Section I — High Alumina Ceramics, 2nd ed., Her Majesty's Stationery Office, London, 1987, p. 87.

[21] A. Kaźmierczak-Bałata, J. Bodzenta, D. Korte-Kobylińska, J. Mazur, K. Gołaszewska, E. Kamińska, and A. Piotrowska, "Determination of thermal conductivity of thin layers used as transparent contacts and antireflection coatings with a photothermal method", *Appl. Optics,* vol.48, no. 7, C74-C80, 2009.

[22] C. R. Wang, and J.M. Yan, "Thermal stability of refractory carbide/boride composites", *Mater. Chem. Phys.*, vol. 74, pp. 272-281, 2002.

[23] R.S. Roth, J.L. Waring, "Phase diagrams for Ceramics", *J. Res. Natl. Bureau Standards Sect A Phys. Chem*., vol. 74, no. 4, p. 487, 1970.

[24] I. G. Talmy, J. A. Zaykoski, and M.M. Opeka, "High temperature chemistry and oxidation of ZrB$_2$ ceramics containing SiC, Si$_3$N$_4$, Ta$_5$Si$_3$ and TaSi$_2$", *J. Am. Ceram. Soc.*, vol. 91, no. 7, pp. 2250-2257, 2008.

Received: September 21, 2009 Revised: October 24, 2009 Accepted: November 6, 2009